Proceedings of the Institution of Mechanical Engineers, Part G: Journal of Aerospace Engineering,
Volume 221, Number 5 (January 2007), pp. 661-678,

Experimental observations of an 8 m/s drop test of a metallic helicopter underfloor structure onto a hard surface: part 1

K Hughes*, **R Vignjevic,** and **J Campbell**
Crashworthiness, Impacts and Structural Mechanics Group, School of Engineering, Cranfield University, Bedfordshire, UK

The manuscript was received on 20 February 2007 and was accepted after revision for publication on 12 June 2007.

DOI: 10.1243/09544100JAERO214

Abstract: This is the first part of a two-part paper that describes the experimental observations for two similar sections of floor that were dropped onto both hard and water surfaces at 8 m/s, as a part of one experimental campaign. The current paper provides an assessment of a simple box-beam underfloor structure typically found in metallic helicopters and provides an overview of the failure modes and the collapse mechanism observed when dropped onto a hard surface. All findings are supported by quantitative measurements and extensive photographic evidence.

The current paper identifies two limitations with the existing design, which are based upon the observations of the failure modes for different frame types and the performance of the intersection joints. In order to increase the level of crashworthiness currently offered, significant frame and joint redesign is required in order to provide a more progressive collapse. The simple buckling modes currently observed should be avoided, as the existing stroke is not fully utilized in the event of a crash, resulting in an inefficient structure. The current paper also discusses the sensitivity to impact angle, as slight variations from a normal impact may result in a detrimental response.

Keywords: crashworthiness, helicopter, testing, hard, failure, design

1 INTRODUCTION

Development of a crashworthy design requires the protection of occupants from severe injuries in potentially survivable crashes, while limiting weight increase, cost, and additional maintenance to acceptable levels. The specifications related to providing sufficent passenger protection in the event of a miltary accident is provided through MIL-STD1210A and the Aircraft Survival Design Guides, which has been superseded by the Joint Service Specifications Guide in 1998 [**1**–**8**].

Structural response of a helicopter airframe to a hard surface impact has been extensively studied in the past as there exists many papers related to this area of research. For example, one of the earliest papers can be found in 1977, which coincides with one of the first studies that employs numerical finite-element analysis to predict the deformation of a skin-covered aluminium frame impacting onto a rigid barrier [**8**].

More recently, significant contribution to the field of helicopter crashworthiness research has been made by Fasanella and Jackson [**9**–**16**], who have not only provided evidence to assess the injury potential of occupants during full-scale hard surface drop tests of composite rotorcraft and fuselage sections, but have also provided extensive guidelines on best practises for crash modelling and simulation [**17**].

In order to attenuate the energy of a crash onto a hard surface, the available stroke of the structure must be used to maximum effect, which involves the harmonious interaction between the landing gear assembly, underfloor structure, energy absorbing seats and the restraint system used by the occupants. This is particularly challenging to engineers because of the reduced stroke available to absorb the impact energy through structural deformation, when compared with their fixed wing counterparts.

**Corresponding author: Crashworthiness, Impacts and Structural Mechanics Group, School of Engineering, Building 52, Cranfield University, Cranfield, Bedfordshire MK43 0AL, UK. email: k.hughes@cranfield.ac.uk*

In order to improve the energy absorbing capabilities of conventional metallic floors, many authors have looked to the development of new materials, together with frame and joint constructions that can promote a stabilized collapse and contribute to energy absorption.

Kindervater [**18**, **19**] has published considerably in the field of composite material model development, the use of composite energy absorbers for crash energy management, together with helicopter crashworthiness. Other solutions previously published consider different frame constructions, such as honeycomb and sinewave beams [**20**], or through the use of triggered composite materials, or specially designed frames that can guide the direction of collapse [**21**].

Consideration has also been given to rivet failure and its effect on the collapse mechanism [**22**], and more recently, the application of optimization stratergies to maximize the energy absorbed for composite and honeycomb structures [**23**]. Retrofit options have also been investigated, by applying composite foams to current fixed wing and rotorcraft, as discussed by Jackson [**24**]. A report on the application of the finite-element method for two metallic subfloor structures for hard and water impacts was published in 2004, which were developed under a NASA contract [**25**].

Modern helicopter crash research has been in the form of collaborative European projects, as the pooling of specialist organization and experimental expertise, are more favourable in attracting funding, which has led to an increase in the number of full-scale experimental test programmes.

Results presented in the current paper were generated as a part of one of these collaborations, in an EU framework V project entilted 'CAST', which is an acronym for Crashworthiness of Helicopters on Water: Design of Structures using Advanced Simulation Tools [**26**]. The outcomes from this project would permit cost-effective design and entry into service crashworthy helicopters for impacts onto hard ground and water. Several papers have been published from this project that includes comparison between test and simulation for component and a full-scale WG-30 airframe [**27**–**29**], as well as the development of a composite subfloor concept that demonstrated an improved crashworthy response on water [**30**].

This two-part paper will compliment existing research, by providing a summary of the experimental observations of a detailed experimental campaign that involved assessing the crashworthiness of a conventional metallic underfloor onto both hard and water surfaces. This would be the first time that a similar section of floor would be dropped during a dedicated expeirmental campaign, and allow the characterization in the response, subject to two extremes in loading (The findings from the water impact scenario is the subject of the second part of this two-part paper.).

This paper provides a complete section-by-section analysis of a simple box-beam structure typically found in metallic helicopters that was taken from the forward part of the main passenger section that encompasses the port and starboard doors of a Westland WG30 helicopter developed in the late 1970s.

The hard surface drop test is described in two sections, with the first providing a description of the test facilities, the choice of boundary conditions and the instrumentation applied to the structure, and the second part will provide a detailed classification of the different failure modes observed. The aim of this research is to provide access to the detailed experimental observations and measurements taken by Cranfield University, which can be used to support future numerical methods validation.

Having a detailed understanding of the collapse mechanism for this type of structure will be critical to understand fully the implications of this design on passenger safety and lead to the identification of potential design improvements for an improved crashworthy response.

2 SUBFLOOR SPECIMEN

The component floor was manufactured from an aluminium 2014 alloy and was taken from the main passenger section of a Westland 16-seater WG30 helicopter. The location of the subfloor relative to the rest of the airframe can be found in Fig. 1.

The subfloor was cut between stations STN1710F and 450F, which is located in the forward part of the main passenger section and corresponds to the full width of the port and starboard doors. This component weighed 44 kg and was 2250 mm wide,

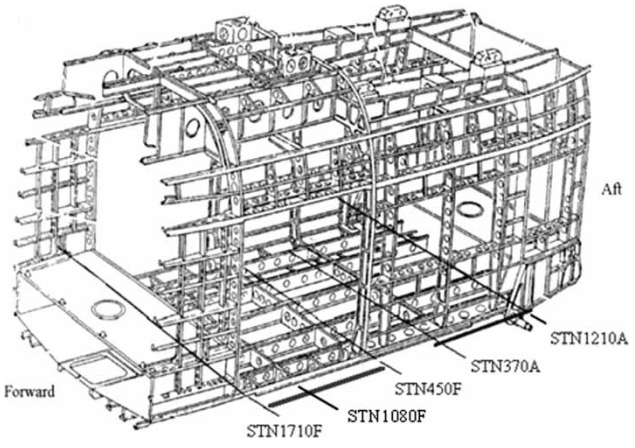

Fig. 1 Location of the component subfloors in relation to the main passenger section of the WG30

1260 mm long and 165 mm high. This section was chosen to investigate the damage that occurs along the section of floor where the main lift frames are directly attached, together with incorporating the influence of at least one other major cross-member (STN1080F). The dimensions of the main structural components can be found in Table 1.

The subfloor is a lattice construction consisting of longitudinal and lateral frames manufactured from metallic sheets, as shown in Fig. 2. The longitudinal 'V' frames are reinforced by three evenly spaced L-section stiffeners and are attached to the upper seat track assemblies with a uniform rivet pitch of 25 mm. The lower parts are reinforced with z-section stiffeners that run fully along their lengths, in addition to providing a riveted attachment to the lower skin.

The 'STN' frames orientated in the transverse direction are also manufactured from metallic sheet and are typically shorter in length. L-section brackets are riveted to the top part of these frames, which provide attachment points for the passenger floor. These transverse frames are connected to the longitudinal frames via C-section overlaps to form individual box-sections. The transverse frames contain a central cutout for a longitudinal z-section stringer that provides structural rigidity for the skin.

The curved end-sections are riveted directly to the main longitudinal end-frames, which provide a direct load path for the main engine and gearbox assemblies to the impacted surface. The passenger section floor is manufactured from a composite material called Fibrelam, which consists of unidirectional glass fibres bonded to a honeycomb/aramid core, which is mounted to the subfloor via tapered screws. The outer skin is also manufactured from metallic sheets and riveted to all longitudinal and transverse frames.

3 HARD SURFACE TEST SETUP

Eurocopter-Deutschland performed this drop test as part of the CAST project, using a steel tower that guided the descent of a trolley to which the component floor was rigidly attached [**31**]. A schematic of the drop test tower, complete with the locations of the instrumentation can be found in Fig. 3. This setup produced the desired near-normal impact velocity of 8 m/s through a 3.26 m free-fall of the trolley–subfloor assembly. The aim of the test is to provide the following information:

(a) global kinematics of the subfloor through accelerometers;
(b) deformation analysis using photogrammetry and laser-displacement sensors – this enables absolute deformation and relative displacement of certain key points, as well as an independent verification of the impact velocity;
(c) high-speed video motion analysis (2000 frames/s at 512 pixels resolution);
(d) post-test photographs of the resulting deformation;
(e) strain gauge data at various locations.

From communication with the helicopter manufacturer, it was decided that frames STN1710F and 450F would support a total mass of 723 kg and that the seat rails situated in between would support 226 kg.

Table 1 Dimensions of the principal components in the floor

Item	Length (mm)	Height (mm)	Thickness (mm)	Thickness (mm)	Material
V830	1292.0	143.0	1.2	2	Al2024
V480	630.0	143.0	1.2	4	Al2024
V0	627.0	143.0	1.2	2	Al2024
STN450F	1655.0	145.0	1.2	1	Al2024
STN450F reinforcement	362.0	145.0	0.9	2	Al2024
STN1710F	2139.0	180.0	0.9	1	Al2024
z-stringer				9	
Web	1300.0	31.0	0.9	–	Al2024
Lower flange	1300.0	18.5	0.9	–	Al2024
Upper flange	1300.0	10.5	0.9	–	Al2024
L-stringers				26	Al2024
Web	20.0	14.0	0.9	–	Al2024
Flange	16.0	14.0	0.9	–	Al2024
Outer skin	1660.0	1272.0	0.7	1	Al2024
Passenger floor	1249.0	326.0	10.0	2	Fibrelam
	1249.0	456.0	10.0	2	Fibrelam
	1249.0	233.0	10.0	2	Fibrelam

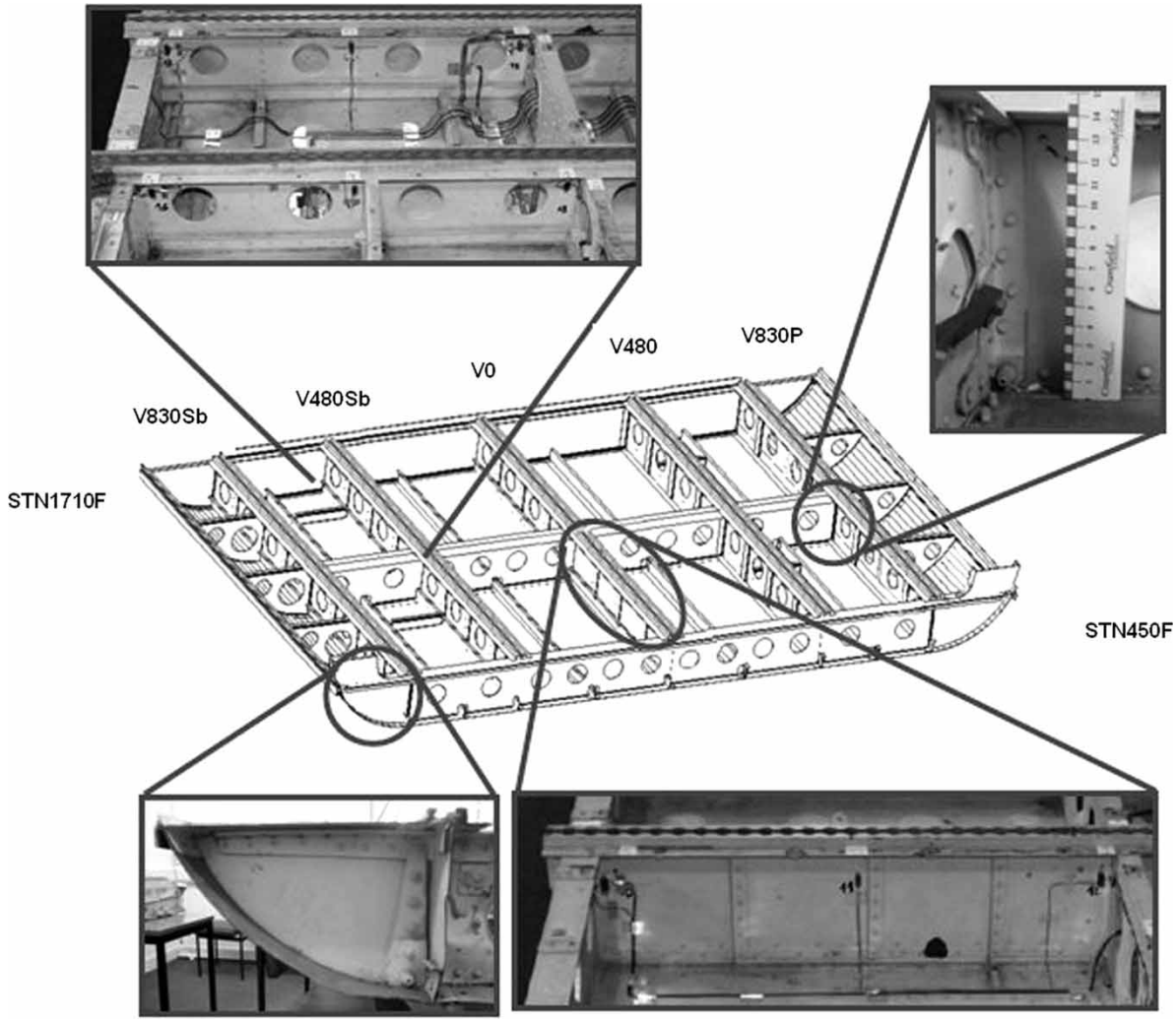

Fig. 2 Schematic diagram showing the nomenclature of the frame numberings used in the current paper, together with close up views of the construction used in the floor

Instead of distributing masses, a decision was made to attach a steel plate across the entire cross-section of the floor. This may be argued as not being representative of the actual boundary conditions that would be experienced, but would ensure, however, that the main features of collapse would be captured. This brought the mass of the test component, including ballast, to 1005 kg.

All instrument data was collected using an NEFF System 620 Conditioner and was filtered using a 1000CFC low pass antialiazing 4-pole Butterworth filter. The location of the accelerometers and the laser displacement sensors, which uses a coordinate system centred at the intersection between V0 and STN450F, can be found in Tables 2 and 3 respectively:

(a) accelerometers, seven in total, with maximum range of 1000 g – these were distributed evenly along frames STN450F, 1710F and the midpoint of V0;
(b) piezoelectric dynamic force sensors, three in total, measuring 800 kN for each plate;
(c) strain gauges, 18 in total, with a measurement range of 40 mm/m (these results have not been discussed in the current paper, but for further information, the reader is referred to the test report [**31**]);
(d) laser displacement sensors, with a measurement range of 400 mm, were rigidly attached to the steel tower in order to provide an estimation of the global vertical displacement after impact (i.e. the rebound behaviour).

4 DEFORMATION SEQUENCE

The impact sequence was captured on three high-speed cameras distributed along STN450F. A sample of the images recorded can be found in Fig. 4, which shows the collapse of the port side of this frame, up

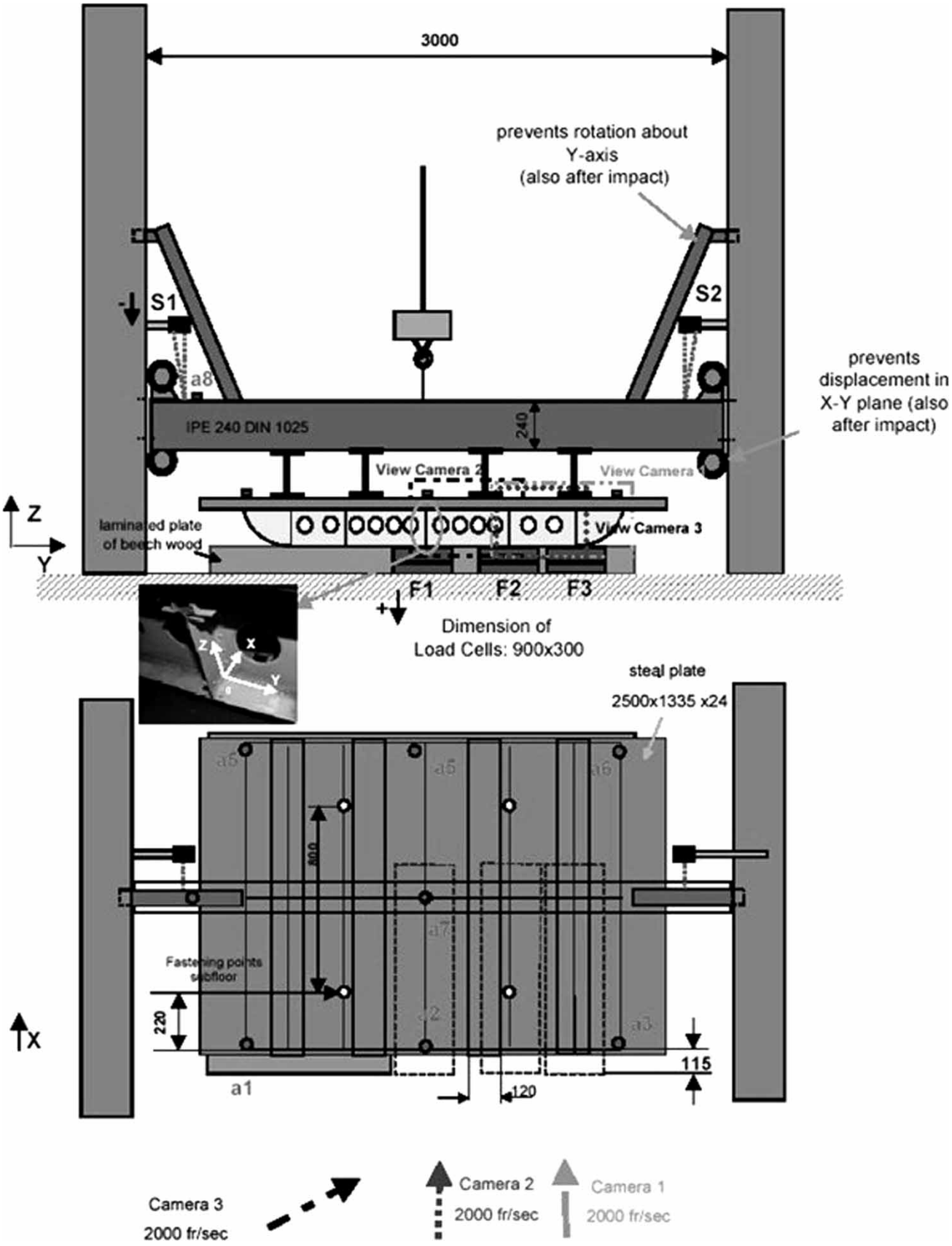

Fig. 3 Schematic representation of the hard surface drop test, which shows the location of the accelerometers, load measurement plates, and high-speed cameras [**31**]

Table 2 Location of the accelerometers in relation to the co-ordinate system centred at the intersection between V0 and STN450F [**31**]

Sensor	Measurement direction	Position (mm)		
		x	y	z
a1	z	−20	−1035	190
a2	z	−20	0	190
a3	z	−20	1040	190
a4	z	1190	−1035	190
a5	z	1190	−35	190
a6	z	1190	1040	190
a7	z	580	0	190
a8	z	580	−1300	670

Table 3 Location of the laser displacement sensors placed on the tower, in relation to the co-ordinate system centred at the intersection between V0 and STN450F [**31**]

Sensor	Measurement direction	Position (mm)		
		x	y	z
S1	z	580	−1325	670
S2	z	580	1325	670

to the point where the first rebound occurs, 14.5 ms after initial contact. As can be seen, there appears to be no observable material failure, as damage is limited to frame folding, coupled with the bending/buckling of the front extension pieces.

5 POST-TEST ANALYSIS

Information was provided on the accelerations at various locations, force-time histories for one half of the subfloor, and a photographic record of the main features of deformation [**31**]. This provided a basic overview of the response of the subfloor to this type of impact, but provided very little in the way of detailed assessment of the performance of different frame constructions, degree of deformation, or the locations of material and rivet failure.

An opportunity arose to the collect the post-impact specimen, which made it possible to perform a detailed frame-by-frame analysis. The condition of the subfloor after impact can be found in Fig. 5, where for clarity, the passenger floor and instrumentation cables have been removed.

To aid orientation, the structure was divided into individual zones, where a local co-ordinate system was defined, which was centred at the intersection between V0 and STN450F, and positive in both the port and forward directions as shown in Fig. 5. All measurements were taken relative to this co-ordinate system, which allowed the absolute relative deformation of the individual plastic hinges to be recorded; the heights of the compacted frames, as well as the displacement of the reinforcing z-stringers, in order to determine the out-of-plane rotation caused by the buckling behaviour of the vertical frames.

The analysis performed as a part of this research aimed to answer the following questions, which will be discussed in turn.

1. What are the main features of a hard surface impact? Are some areas more susceptible to damage than others?
2. Assess the effectiveness of the intersection joints that form between longitudinal and transverse members.
3. Assess the behaviour of the skin and its role in energy absorption.
4. Identify the main locations of rivet and material failure.
5. Assess the behaviour of the curved end-sections (skin and frames).

6 MAIN FEATURES OF A HARD SURFACE IMPACT

Despite the separation of STN1710F, the subfloor remains intact, with deformation observed in all longitudinal and transverse members, which is consistent with the nature of the distributed loading applied to the cross-section of the floor, due to the presence of the steel ballast plate. The degree of frame deformation is strongly influenced by its construction, as will be discussed in the next section.

One of the main features to note from the global view in Fig. 5 is the fact that the deformation is not uniform, as it is more severe towards the front half of the component between stations 1710F and 1080F. This asymmetry is caused by the separation between STN1710F and the rest of the subfloor. This loss in localized strength reduces the load-carrying ability in this region, permitting more deformation in the form of increased material failure and severity of the magnitude of the plastic hinges. Figures 6 and 7 provide a more detailed view of the damage to the forward and aft sections respectively, where only the port side is considered due to the similarities in the transverse direction either side of frame V0.

Very little deformation occurs at the doorframe attachment points located at the forward and aft sections of V830 port and starboard. This section is reinforced along both sides by reinforcing brackets, as well as with an I-beam section along its midpoint, as shown in Fig. 8. The lack of deformation is as expected, as the substantial nature of the construction will result in a higher collapse load when compared to the other frames in the floor. It is expected that this increase in failure strength at this location would result

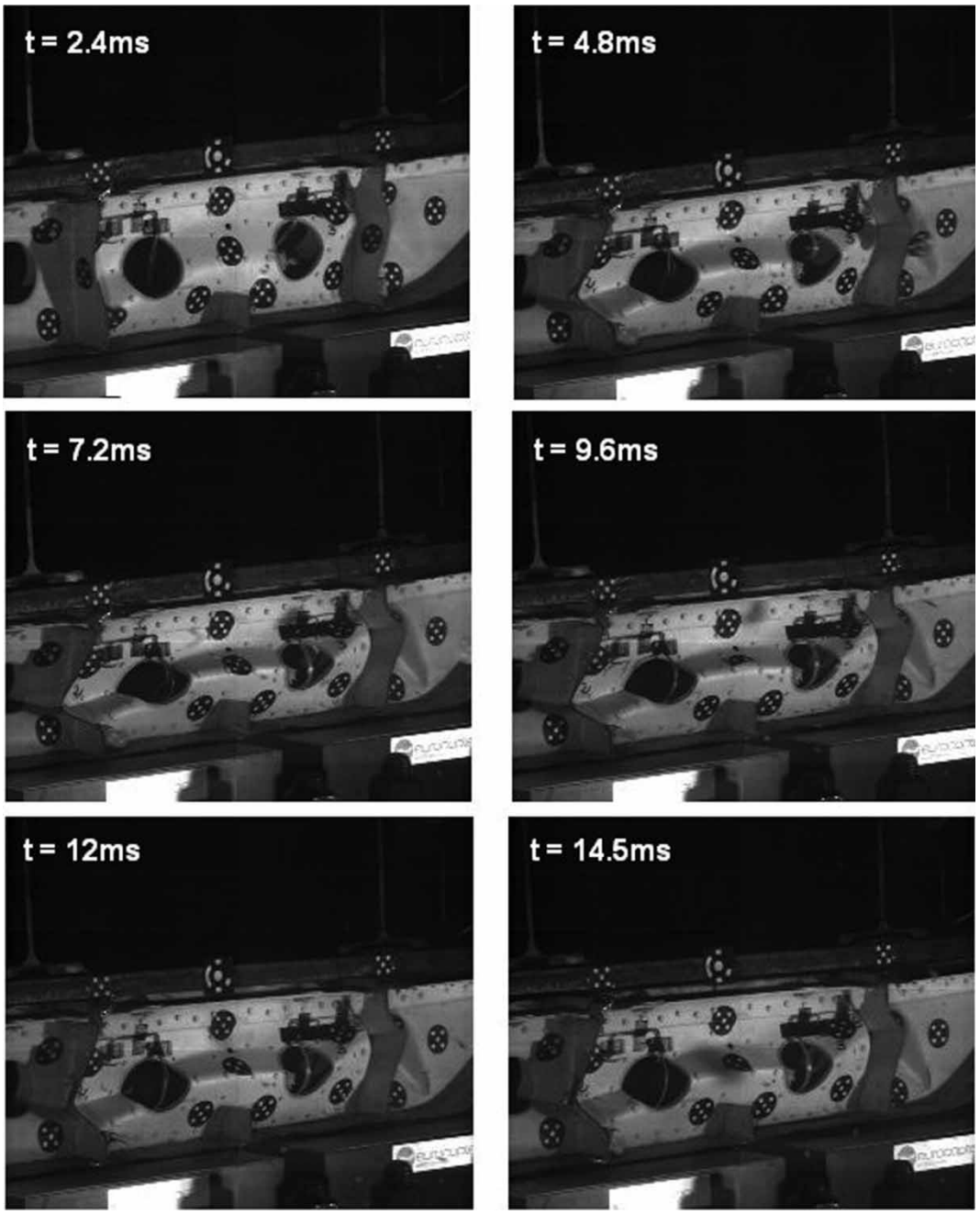

Fig. 4 Deformation sequence of STN450F up to the point of the first rebound, which occurs at $t = 14.5$ ms

in localized buckling in the main lift frames that are directly attached, due to the action of supporting the overhead masses.

7 FRAME CONFIGURATIONS AND THEIR FAILURE MODES

Classification of frame response has been split into three sections that correspond to the different constructions used. The failure modes for the longitudinal frames V0, V480, and V830 can be found in Figs 9 to 11, where the dotted and solid lines denote the locations and directions of the plastic hinges in the positive and negative y-directions respectively:

(a) frame without holes (i.e. V0);
(b) frame with holes (i.e. V480P and S);
(c) end-frames with holes (i.e. V830P and S).

7.1 Configuration no. 1 – V0

The section of V0 situated between STN1080F and 450F, consists of a single metallic sheet to which three

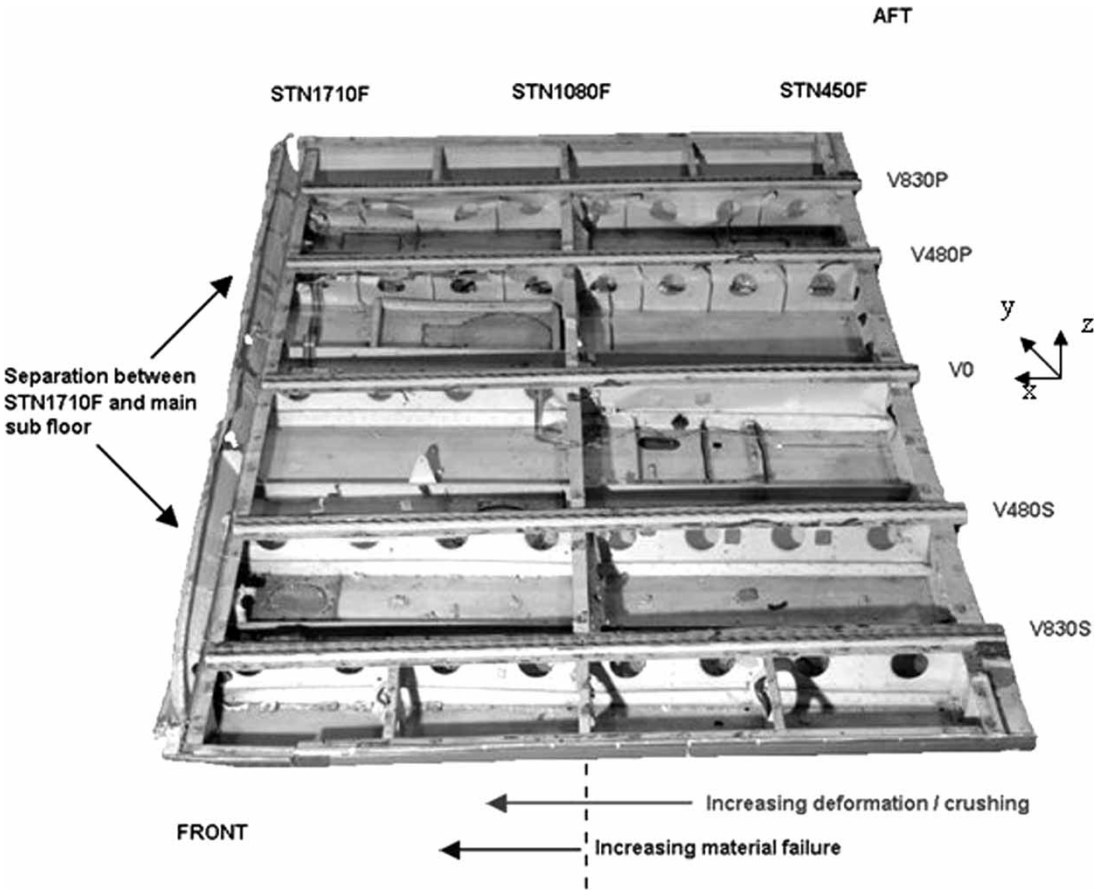

Fig. 5 Global view of post-test article where the instrumentation and passenger floor have been removed for clarity

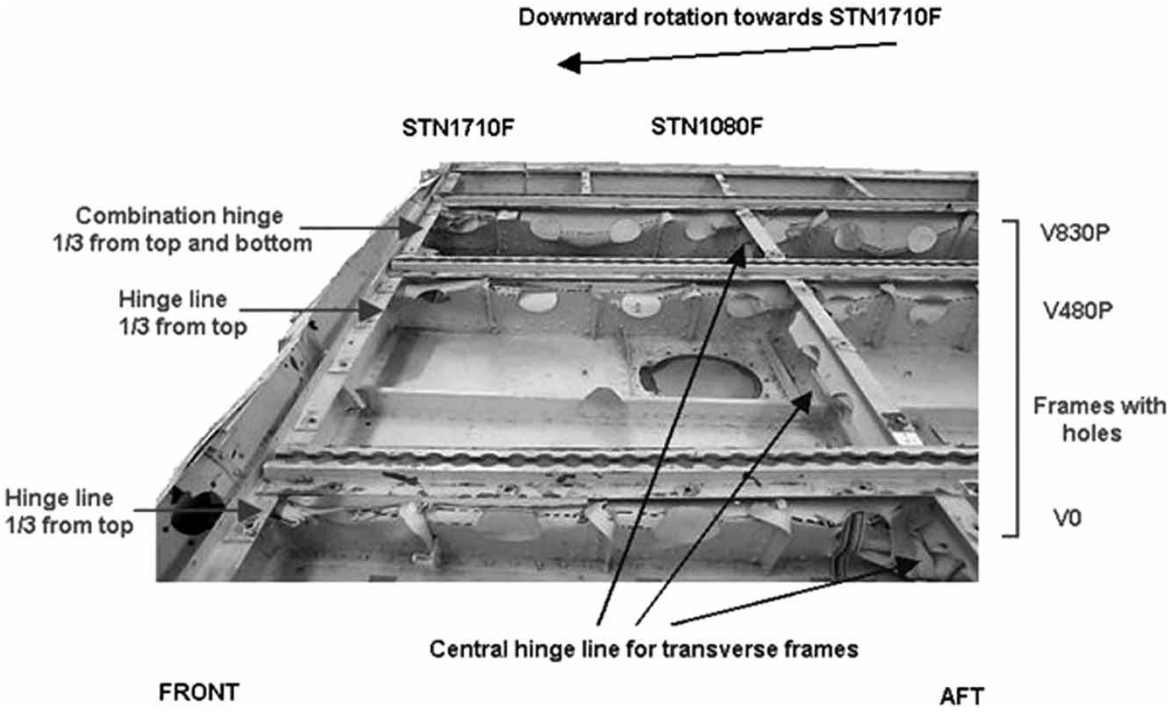

Fig. 6 Forward port side deformation observed between frames V0 and V830P

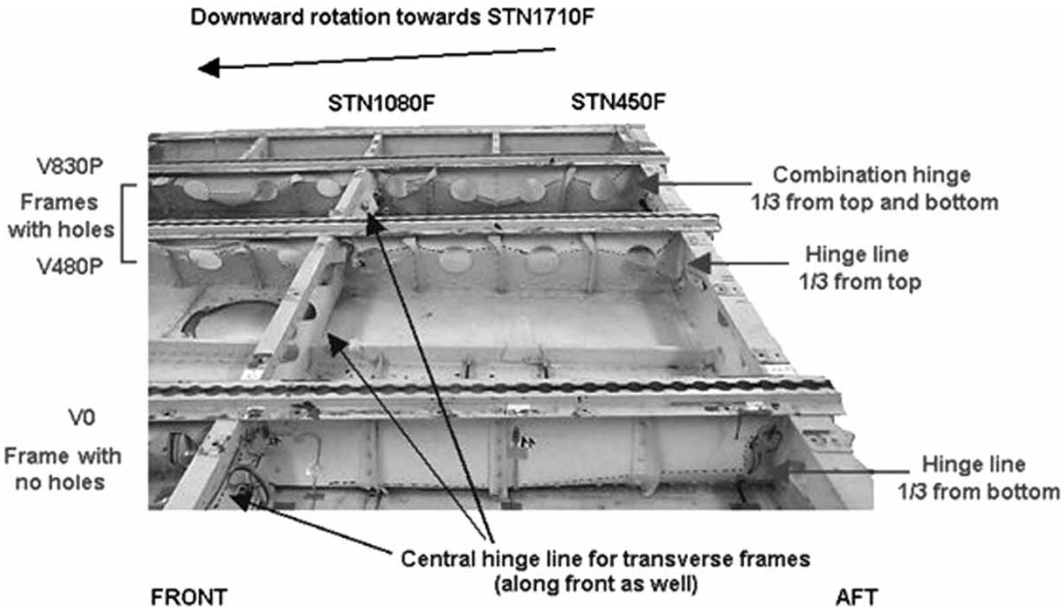

Fig. 7 Aft port side deformation observed between frames V0 and V830P

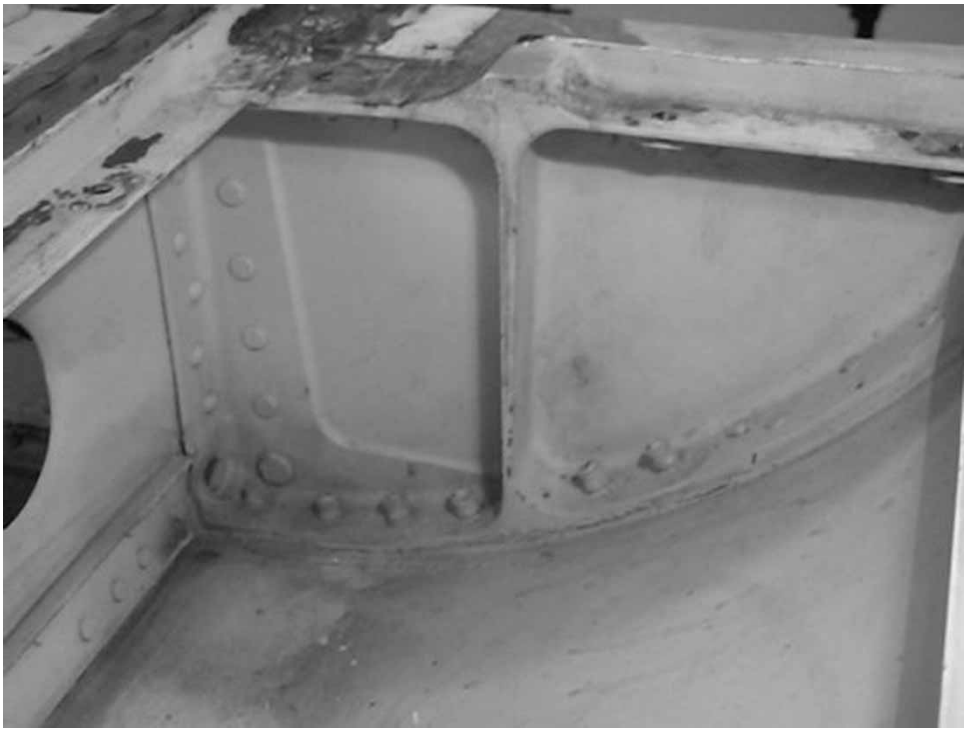

Fig. 8 Interior view of the starboard doorframe attachment point, which shows the degree of reinforcement incorporated into the design

L-section stringers are directly attached. Riveted to the base, on the opposite side shown in Fig. 9, is a z-section stringer. The failure mode of this frame consists of a single hinge line that forms in the lower part of this frame, at a height corresponding to the top of the z-stringer. This positive outward buckle in the *xz*-plane results in the vertical stringers also adopting this failure mode, causing small-localized material fractures at the location of peak z-stringer deflection.

7.2 Configuration no. 2 – V480P

This frame configuration is the most common and consists of a single metallic sheet that is riveted to

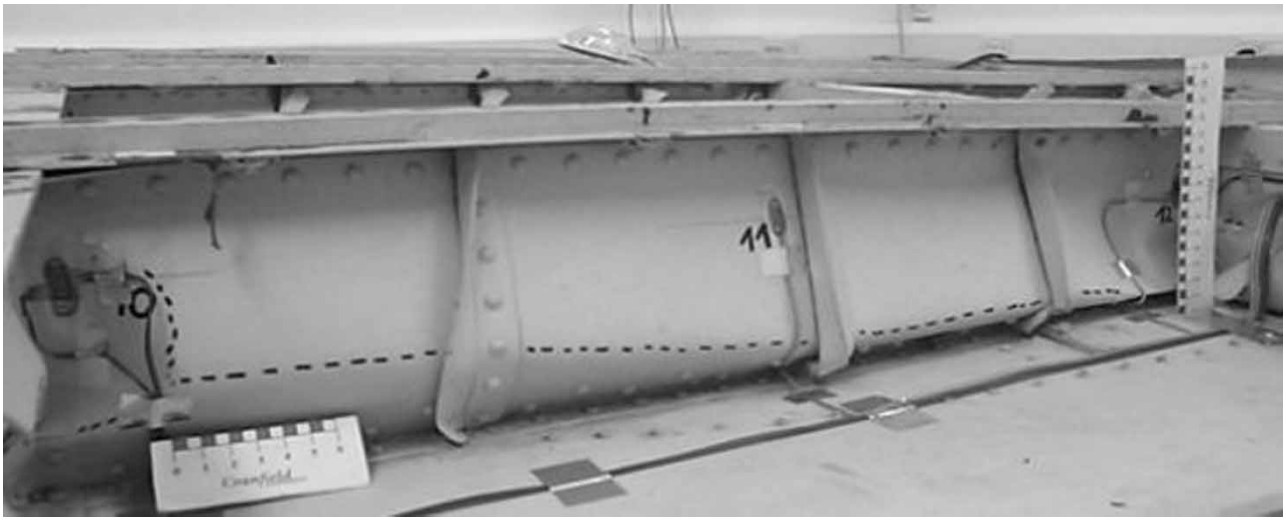

Fig. 9 Global view of the failure mode for frame configuration no. 1, V0

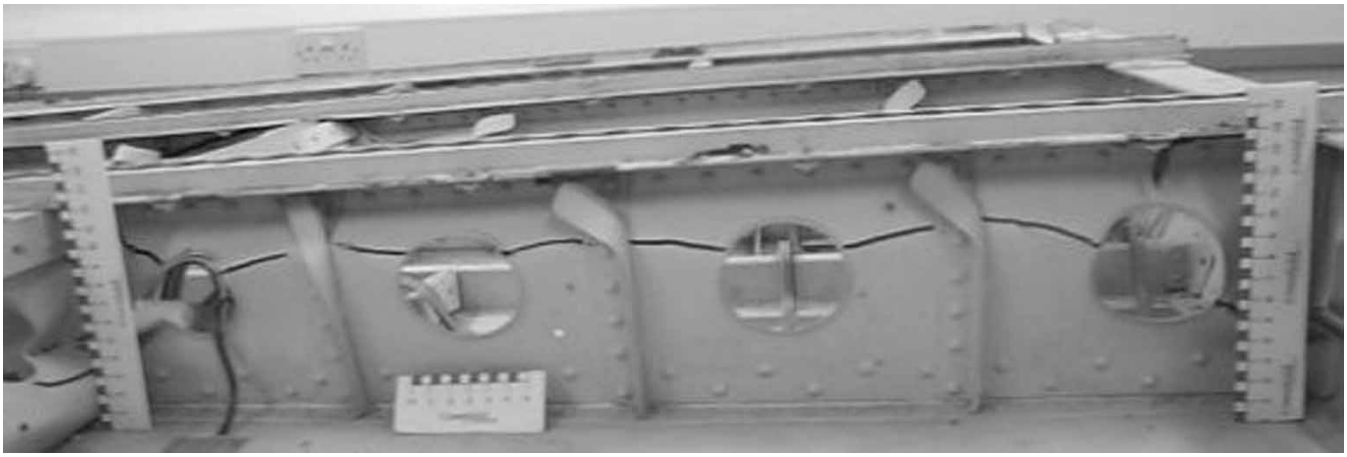

Fig. 10 Global view of the failure mode for frame configuration no. 2, V480P

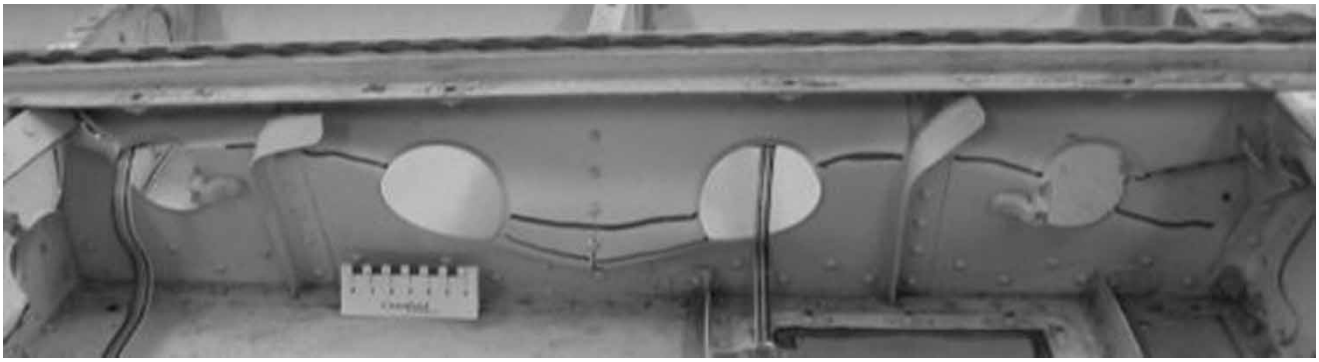

Fig. 11 Global view of the failure mode for frame configuration no. 3, V830P

the transverse frames. The frame is also reinforced with evenly spaced vertical L-section stringers and also contains four circular cutouts that act to reduce the weight of the frame, while allowing the routing of hydraulic piping, electrical cables, etc.

The failure mode is opposite to configuration no. 1, as the dominant hinge line forms in the upper part of this frame, because of the high-stress concentrations around the cutouts. The vertical stringers reinforce this frame and deform in the positive x-direction, at a location corresponding to the peak deflection of the main plastic hinge line.

7.3 Configuration no. 3 – V830P

The final frame configuration is similar in construction to configuration no. 2, except this frame does not have a vertical stringer located at the midpoint. Instead, this frame is directly riveted to a curved transverse end-frame, which provides the vertical support. Despite construction being similar, the failure mode is a combination of the other two configurations, as hinge lines form in both the top and lower parts of the frame. The difference in failure mode can be attributed to the end-section providing a buckling trigger that causes this large out-of-plane deflection and the lower hinge that is observed.

A comparison between the compacted heights for all three-frame configurations can be found in Fig. 12, which clearly demonstrates an increase in deformation towards the aft part of the subfloor, which is a direct consequence of the separation of STN1710F. This increase in deformation is caused by the remainder of the supporting structure absorbing the rest of the loading.

There is also a slight asymmetry between the port and starboard displacements, which is particularly evident for V830, as the results differ by up to 10 mm. This discrepancy could be caused by a number of reasons. For example, there could be a slight eccentricity in the impact angle resulting in this section of the floor taking more of the loading, or the separation of STN1710F may have caused a significant change in the load path.

8 INTERSECTION JOINTS

The collapse of a box-section is heavily dependant upon the behaviour of the supporting frames, together with the collapse of the intersection joints. As these regions are inherently strong due to the number of plies that are riveted together, an understanding of their behaviour with respect to energy absorption is particularly important for improving the level of crashworthiness currently offered.

During a hard surface impact, the intersection joints together with the reinforcing L-stringers stabilize the collapse mechanism by providing support to the connecting frames that buckle under the loading. As can be seen in Fig. 13, the intersection joints also absorb part of the impact energy by buckling. The reduced height of the joints are small, with heights differing by up to (15 ± 1) mm, which indicates that very little energy is being absorbed with the current design.

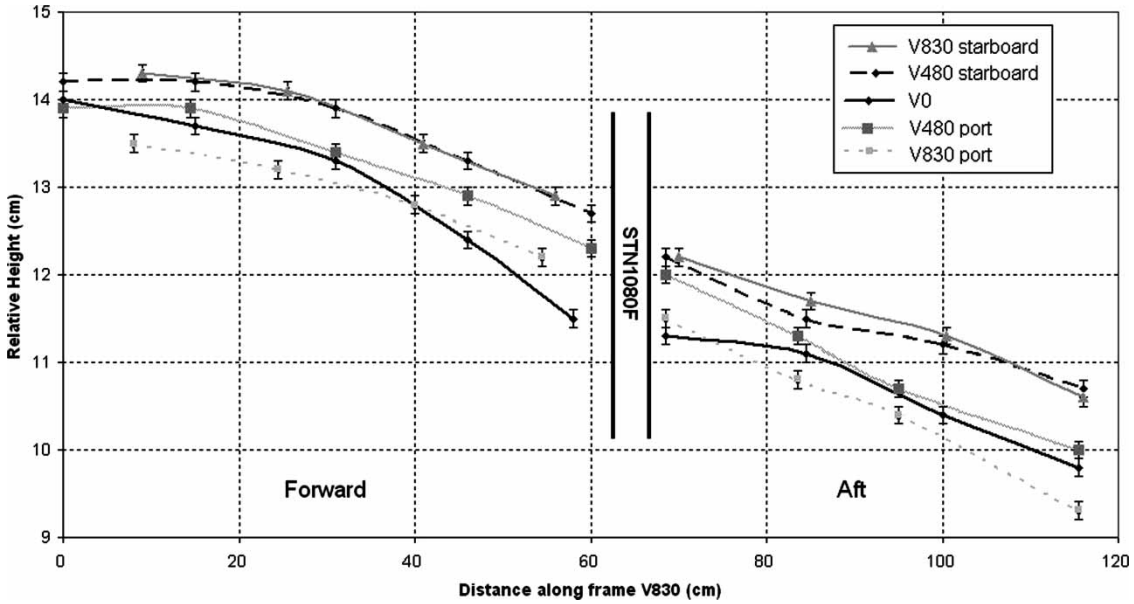

Fig. 12 Variation in height of the upper seat track assembly along V0, V480, and V830, as a function of the distance along the frame towards STN1710F

Fig. 13 Behaviour of a typical intersection joint for a hard surface impact (V0 and transverse mid-frame)

This indicates that joint design is one area where significant development should occur, either through a change in geometry and/or the inclusion of a trigger in order to take advantage of the stroke that is potentially available. The progressive failure of these joints will be critical to allow increased and controlled frame collapse.

9 SKIN BEHAVIOUR AND ITS CONTRIBUTION TO ENERGY ABSORPTION

As expected, the skin plays no role in the energy absorbing process and remains primarily undeformed. The only observed damage occurs along the boundary between the curved end-sections and the ground, due to the compression of the hinge line that forms, as shown in Fig. 14.

10 LOCATIONS OF RIVET AND MATERIAL FAILURE

STN1710F is riveted to the upper seat track assembly, to which the steel loading plate was directly attached.

Fig. 14 Localized skin-material failure that occurs along the curved end-section of the skin at the intersection with STN1710F

The failure of these rivets did not occur upon contact, as the frame deforms in response to the impact loading as Fig. 15 demonstrates. It is clear to see the dominant plastic hinge line that forms (dashed circles), which results in the buckling of the two halves of this frame at the intersection with V0 and the failure of the interconnecting rivets (solid circle).

Shear failure of the rivets attaching STN1710F to the aft part of the component floor was attributed to a change in load path caused by a rotation of the steel loading plate around the central connecting I-beams of the guided trolley assembly. The cause of this rotation was due to an unexpected flexibility of the joints connecting the four transverse I-beams in Fig. 3 and the central guided I-beam. It was assumed that these connections would be rigid, which was not the case upon post-processing the results. This rotation was unexpected, as the test rig was designed to constrain movement in the vertical direction only. This rotation was detected through laser-displacement sensors tracking the motion of the steel plate in Fig. 16, together with the asymmetry of the damage observed. The velocity time histories were obtained from the displacement results and can also be found in Fig. 16. Despite the differences recorded by the two lasers, the results provide well-defined markers for when the floor is brought to rest, as the rebound occurs between 12.5 and 20 ms, which corroborates what is observed by the high-speed cameras.

Separation of STN1710F influences the collapse by causing the surrounding structure to support the rest of the impact loading. This produces several locations of material and rivet failure as shown in Figs 17 and 18. The visual difference in compacted height of V480 port between SN1710F and 1080F is clearly shown in Fig. 17, where localized material failure increases in severity towards the intersection with STN1710F. This change

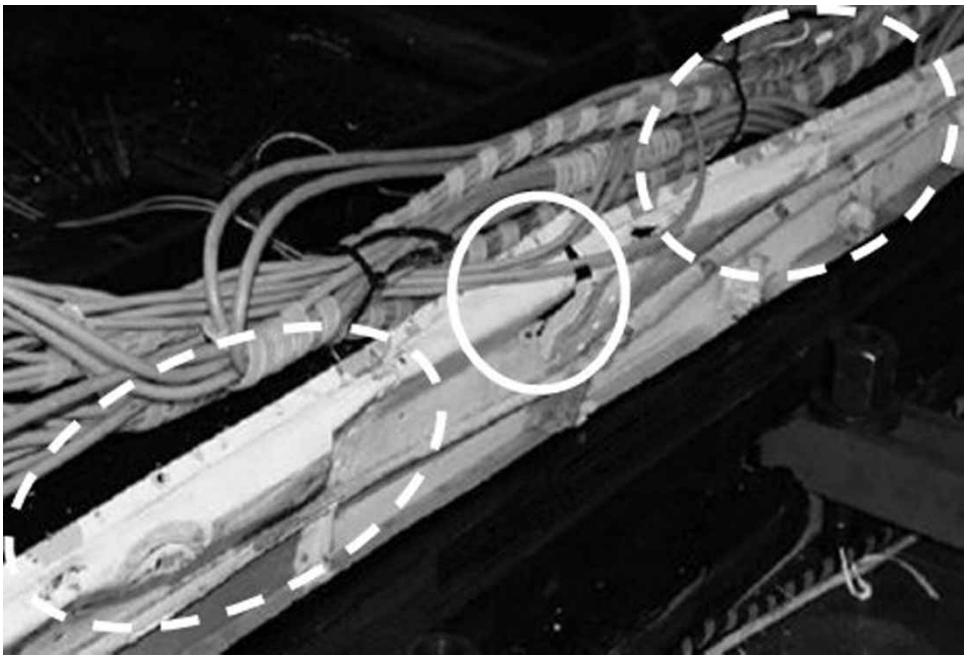

Fig. 15 Isometric view of STN1710F showing the location of the dominant plastic hinge line (blue) and the failure of the rivets (red)

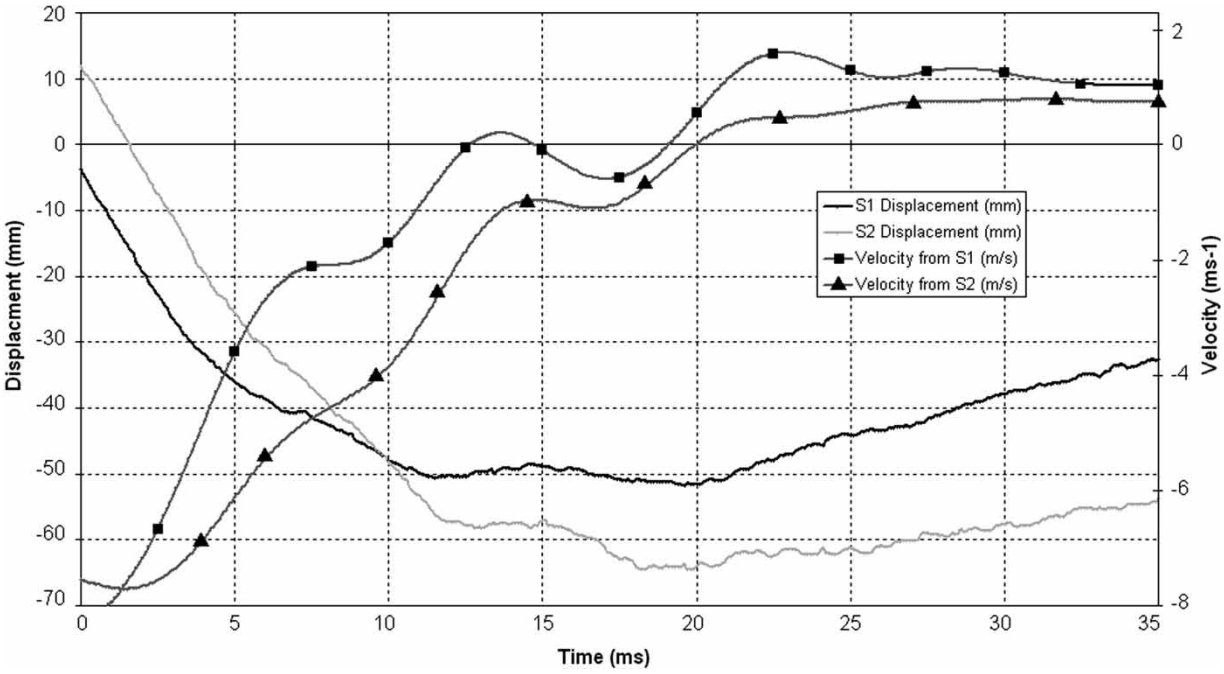

Fig. 16 Comparison between the displacement–time histories obtained from laser displacement sensors S1 and S2, and the corresponding velocity–time curves obtained from these results

in failure mode and the resulting separation significantly affects the balance of the loading either side of STN1080F in Fig. 12, where the relative difference in height between the forward and aft most points of the rails varies between 2 and 4 cm.

A coarse estimate of this rotation was obtained using the relative heights of the upper seat tracks for the longitudinal frames V0, V480, and V830 presented in Fig. 12. However, using this data alone will underestimate the rotation due to the separation of the upper rail assembly with STN1710F.

In order to approximate the maximum vertical deflection of the steel plate, it was necessary to study the surrounding damage. There is evidence from

Fig. 17 Aft section of V480P showing the difference in height at the intersection with STN1080 (left) and STN1710 (right)

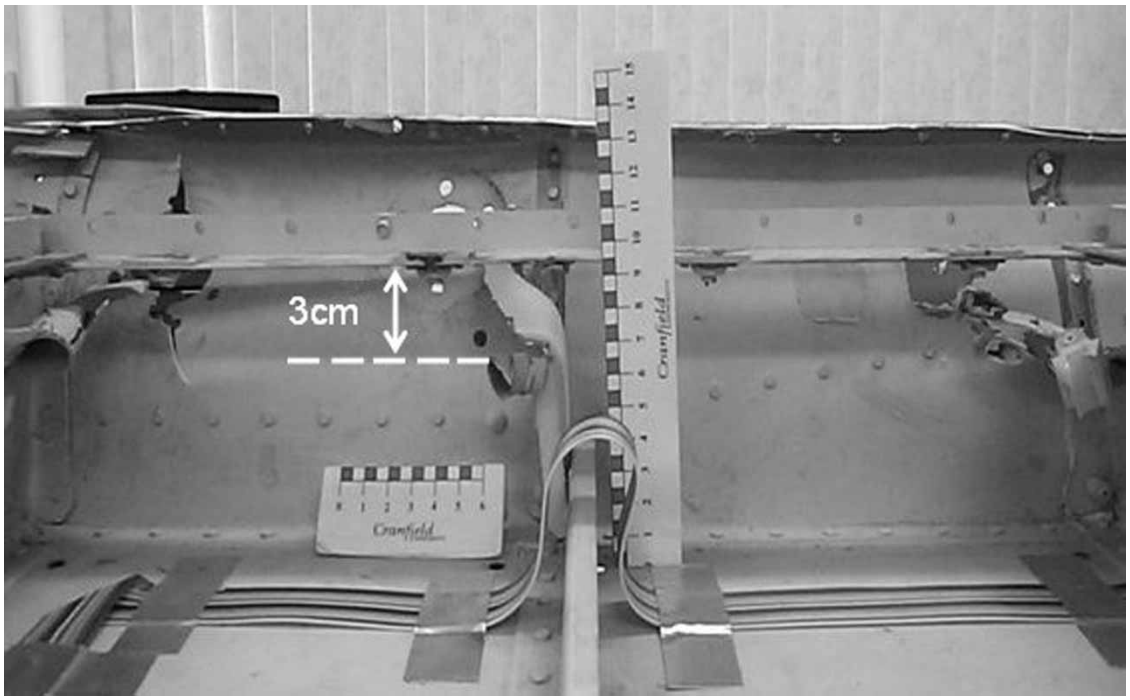

Fig. 18 STN1710F located between frames V0 (left) and V480S (right)

Table 4 Estimation of the total rotation of the steel plate based upon the final height of the seat track assembly and the estimated degree of travel before unloading to its final deformed position

Frame	Location	ΔL (± 0.1) cm	ΔH (± 0.1) cm	Maximum degree of travel (± 0.2) cm	Rotation estimate (degrees)
V830	Starboard	107.0	−3.7	−6.7	-3.6 ± 0.1
	Port	107.5	−4.2	−7.2	-3.8 ± 0.1
V480	Starboard	116.0	−3.5	−6.5	-3.2 ± 0.1
	Port	115.5	−3.9	−6.9	-3.4 ± 0.1
VL0	Centreline	115.5	−4.2	−7.2	-3.6 ± 0.1

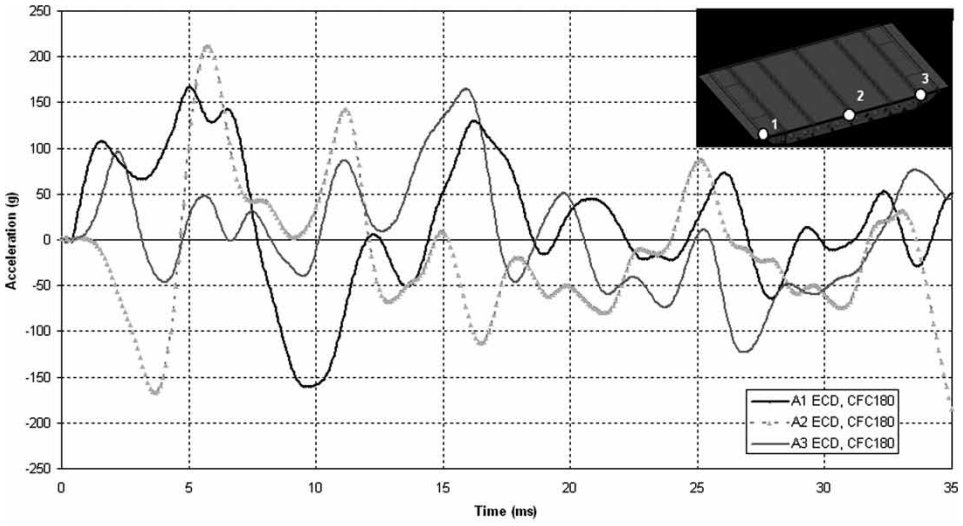

a

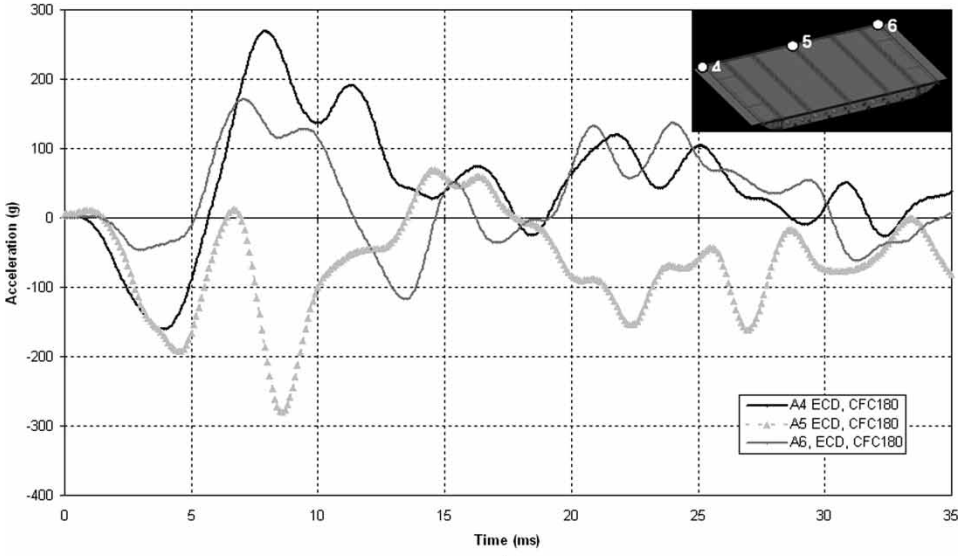

b

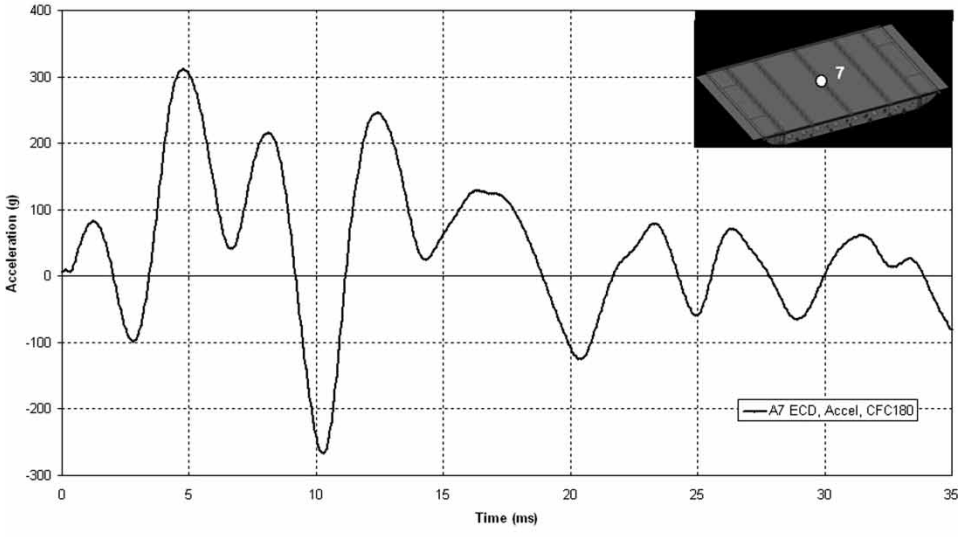

c

Fig. 19 Experimental acceleration–time histories for A1 through A7

Fig. 17 that material fracture in the longitudinal frames has enabled the upper seat track to travel further, which has been estimated using the deformation of the surrounding components shown in Fig. 18. This photograph suggests that the seat rail has travelled a further 30 mm due to the tearing of the vertical supporting member, before elastically unloading to its final deformed height.

Combining this change in height with the estimated travel of the seat track assembly has enabled estimates for this rotation to be calculated as shown in Table 4. The average value for this rotation was (3.5 ± 0.1) and has resulted in quite a significant effect on the resulting damage, as the drop test has no longer recreated the case of uniform loading.

The behaviour of the three frame types are also evident in the aft section of the floor, where the increase in deformation represents a more extreme response and provides a valuable insight into understanding the consequences of the potential failure mechanisms. The current design shows limited energy absorption, as once a dominant hinge line forms, the construction as a whole is not operating effectively due to a complete loss in frame stiffness, which represents a significant limitation with the existing metallic design.

11 ACCELEROMETERS

It was originally intended to place seven evenly spaced accelerometers along the seat rails of frames STN450F, V0, and STN1710F. During setup however, the accelerometers were directly attached to the top surface of the steel plate, presumably out of ease from an experimental point of view. The time histories in Fig. 19 shows that there appears to be no consistency between traces, as the signals are extremely noisy, even when low frequency CFC60 filters are applied.

What is also interesting is the fact that the traces appear to be out of phase, especially, when you consider the behaviour at the ends and centre of the plate. Due to the repeatability observed, this infers that the traces are being compounded by the vibration of the steel plate, especially at the centre (A7). The time period of this oscillation is approximately 3 ms, which equates to a frequency of 330 Hz.

A closer analysis of the high-speed video footage shows the movement of the steel plate as consisting of a combination of rotation, as well as vibrational oscillations that are particularly pronounced at the extremities. Due to the flexure that is observed, the steel plate is not behaving as a rigid body, resulting in noise being superimposed onto the signal. Therefore, it has not been possible to infer any conclusions from these results.

12 FORCE–TIME HISTORIES

A comparison between the force–time histories obtained for dynamic piezoelectric force sensors F1, F2 and F3 defined in Fig. 2, can be found in Fig. 20.

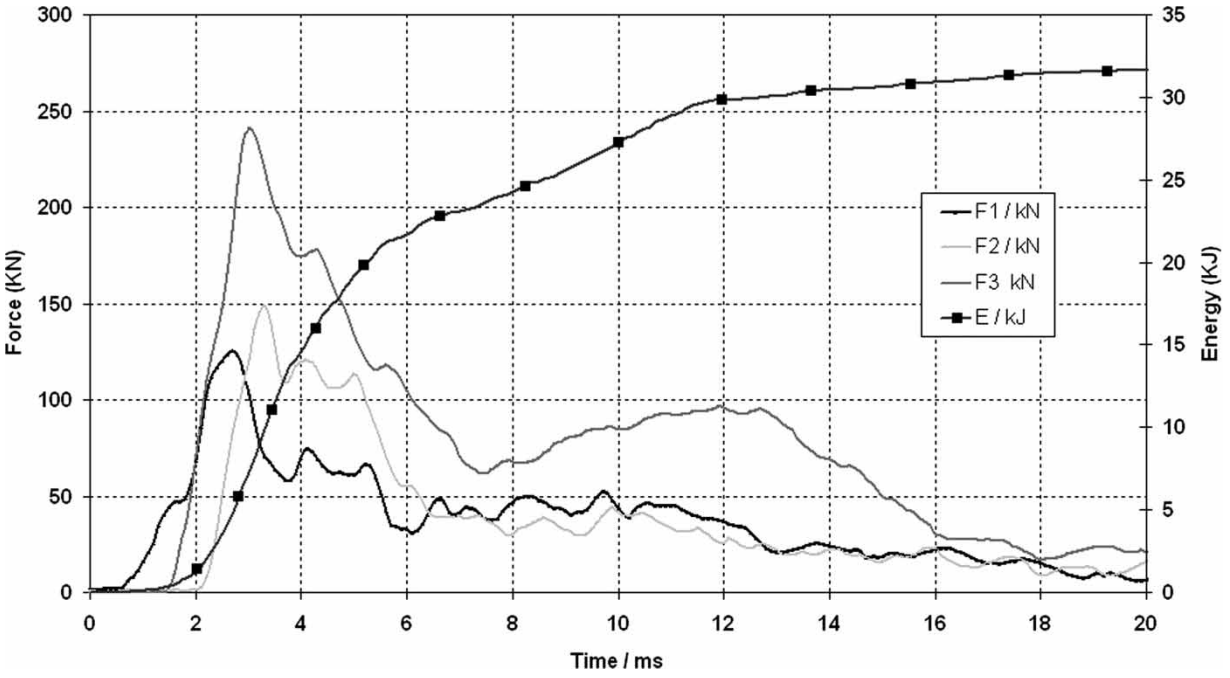

Fig. 20 Comparison between the force–time histories obtained for the three dynamic force sensors F1, F2, and F3. Also plotted is the global energy absorbed by the structure, which was obtained from the force and displacements measurements recorded during the drop test

The magnitudes for the peak force for F1 and F2 are similar, ranging from 120 to 150 kN, whereas the peak force recorded for plate F3 is much larger at 240 kN.

This increase in the measured force at F3 is expected, due to the substantial nature of the construction along V830, coupled with the reinforcements that are present in Fig. 8. This lack of deformation, when compared to frames V480 and V0 is accountable for the difference in the peak force observed. For all three locations, the force reduces to a sustained level between 6 and 12 ms, before reducing effectively to zero after 18 ms.

Combining the data from the laser displacement sensors and extrapolating the force results to obtain the global force–time history, the total energy absorbed by the floor can be estimated. With a combined floor and ballast mass of 1005 kg and an impact velocity of 8 m/s, the initial kinetic energy to be absorbed equates to 32 kJ. The energy–time history is plotted in Fig. 20, which shows that all the impact energy has been absorbed through structural deformation.

From the force–time histories and the frame failure mechanisms observed, it is clear that improvements could be made by providing a more progressive collapse front through considering different frame construction, triggers, and material type, as opposed to the single dominant hinge line currently observed. The bulk of the energy absorbed is within the first 12 ms as shown in Fig. 20, after which, there is little further increase due to a reduction in the load-carrying ability offered by the structure once failure occurs. This modification would result in a higher collapse load in the region of deep collapse and increase in the energy absorbed plastically by the structure.

13 CONCLUSIONS

Detailed examination of the post-test specimen presented in the current paper aims to provide an understanding of the response of a typical metallic underfloor structure to an impact on a hard surface by identifying its failure modes. The following is a summary of the main findings.

The existing structure is capable of absorbing the energy of the impact, as the response of the subfloor is consistent with the current understanding, as all vertical components fail in buckling and the skin plays no role in the energy absorbing process. This is an inefficient way of utilizing the stroke that is available, as once the dominant hinge line forms, the strength is severely reduced and the frame can no longer support the impact loads or absorb further energy.

Depending upon the nature of the construction, three different frame responses have been identified. In all cases, small-localized fractures appear in the vertical reinforcing stringers, corresponding to the height of the dominant hinge line that forms.

1. Frames manufactured from a single sheet will develop a single hinge line that corresponds to the height of the reinforcing z-stringer that runs along its base.
2. The second type consists of a single sheet with four circular cutouts. The hinge line forms in the upper part of the frame, due to the high stress concentrations that form around these holes.
3. The final configuration is similar to type two, except the frame is reinforced at its midpoint by a transverse end-section. This provides a buckling trigger, so hinge lines are a combination of the other two failure modes, with plastic hinges forming in both the top and lower parts of the frame.

Due to the flexibility of the steel loading plate and its connections, the drop test did not recreate the desired near normal impact, but did allow two extremes in response to be captured, providing a better understanding of the failure mechanism for this typical construction. The results demonstrate that the collapse mechanism is sensitive to variations in impact angle, as the introduction of a non-uniform load is likely to produce severe damage and localized frame failure. Once this occurs, the frame cannot support the loading, resulting in a change in load path and potential failure of other components.

The joints are an important part of the collapse as they provide support to the end-sections of the frames. These intersection joints also buckle under the loading, but the limitation with this design is the high failure strength that is required to initiate collapse. It would be beneficial to redesign these joints to encourage a more progressive collapse, as opposed to the simple buckling mode that is currently observed.

There are two design issues that need to be addressed; the first is that consideration should be given to frame design to ensure progressive collapse through the careful design of geometry, material type and the inclusion of a trigger, and the second is through the redesign of the joints. The progressive failure of these joints will be critical to allow increased and controlled frame collapse. Both issues will have to be addressed in order to improve the crashworthiness of future metallic underfloor designs.

ACKNOWLEDGEMENTS

This work was performed within the project CAST, which is funded by the European Community under the Competitive and Sustainable Growth programme (Contract G4RD-CT1999-0172). The drop test was

performed by Eurocopter-Deutschland as part of this project.

REFERENCES

1 **Military Standard, MIL-STD01210A.** Light fixed and rotary wing aircraft resistance. Department of Defense, Washington DC, September 1988.

2 *Aircraft crash survival design guide*, vol. I – Design criteria and checklists. USAAVSCOM TR 89-D-22A, December 1989 (Simula Inc., Phoenix, AZ).

3 *Aircraft crash survival design guide*, vol. II – Aircraft design crash impact conditions and human tolerance. USAAVSCOM TR 89-D-22B, December 1989 (Simula Inc., Phoeneix, AZ).

4 *Aircraft crash survival design guide*, vol. III – Aircraft structural crash resistance. USAAVSCOM TR 89-D-22C, December 1989 (Simula Inc., Phoeneix, AZ).

5 *Aircraft crash survival design guide*, vol. IV – Aircraft seats, restraints, litters and cockpit/cabin delethalization. USAAVSCOM TR 89-D-22D, December 1989 (Simula Inc., Phoeneix, AZ).

6 *Aircraft crash survival design guide*, vol. V – Aircraft post crash survival. USAAVSCOM TR 89-D-22E, December 1989 (Simula Inc., Phoeneix, AZ).

7 *Joint service specification guide. Crash protection handbook*, JSSG-2010-7, 30 October 1998.

8 **Winter, R., Pifko, A. B.,** and **Armen, H. Jr** Crash simulation of skin-frame structures using a finite element code. SAE paper 770484, 1977.

9 **Jackson, K. E.** and **Fasanella, E. L.** Development of a 1/5 scale model fuselage concept for improved crashworthiness. In Symposium on Size Effects and Scaling Laws, 13th US National Congress on Applied Mechanics, Gainesville, FL, 21–26 June 1998.

10 **Jackson, K. E.** and **Fasanella, E. L.** Crashworthy evaluation of a 1/5-scale model composite fuselage concept. NASA/TM-1999-209132, ARLMR-441, US Army Research Laboratory, Langley Research Centre, Hampton, Virginia, April 1999.

11 **Jackson, K. E.** and **Fasanella, E. L.** Impact testing and simulation of a crashworthy composite fuselage. American Helicopter Society 56th Annual Forum, Virginia Beach, Virginia, 2–4 May 2000.

12 **Fasanella, E. L., Jackson, K. E.,** and **Lyle, K. H.** Finite element simulation of a full-scale crash test of a composite helicopter. American Helicopter Society 56th Annual Forum, Virginia Beach, Virginia, 2–4 May 2000.

13 **Sareen, A. K., Fasanella, E. L., Sparks, C., Jackson, K. E.,** and **Mullins, B. R.** Comparison of hard surface and soft soil impact performance of a crashworthy composite fuselage concept. American Helicopter Society 58th Annual Forum, Montreal, Canada, 11–13 June 2002.

14 **Fasanella, E. L.** and **Jackson, K. E.** Impact testing and simulation of a crashworthy composite fuselage section with energy-absorbing seats and dummies. NASA TM-2002-211731 ARL-TR-2734, 202.

15 **Jackson, K. E., Fasanella, E. L.,** and **Boitnott, R.** Occupant responses in a full-scale crash test of the Sikorsky ACAP helicopter. American Helicopter Society 58th Annual Forum, Montreal, Canada, 11–13 June 2002.

16 **Jackson, K. E., Fasanella, E. L., Boitnott, R. L.,** and **Lyle, K. H.** Full-scale crash test and finite element simulation of a composite prototype helicopter. NASA/TP-2003-212641, ARL-TR-2824, August 2003.

17 **Fasanella, E. L.** and **Jackson, K. E.** Best practises for crash modelling and simulation. NASA/TM-2002-211944, October 2002.

18 **Kindervater, C. M.** Aircraft and helicopter crashworthiness: design and simulation. In *Crashworthiness of transportation systems: structural impact and occupant protection* (Ed. J. A. C. Ambrosio), 1997, pp. 525–577 (Kluwer Academic Publishers, The Netherlands).

19 **Kindervater, C. M.** Trends in simulation – helicopter and aircraft structures under extreme crash and high velocity impact. Annual Forum Proceedings, American Helicopter Society International, 2005, vol. 2, pp. 1502–1513.

20 **Vicente, J. L. S., Beltran, F.,** and **Martinez, F.** Simulation of impact on composite fuselage structures. In European Congress on Computational Methods in Applied Science and Engineering (*ECOMAS*), Barcelona, September 2000.

21 **Taher, S. T., Mahdi, E., Mokhtar, A. S., Magid, D. L., Ahmadun, F. R.,** and **Arora, P. R.** A new composite energy absorbing system for aircraft and helicopter. *Compos. Struct.*, 2006, **75**, 14–23.

22 **Bisagni, C.** Crashworthiness of helicopter under floor structures. *Int. J. Impact Eng.*, 2002, **27**(10), 1067–1082.

23 **Lanzi, L., Bisagni, C.,** and **Ricci, S.** Neural network systems to reproduce crash behaviour of structural components. *Comput. Struct.*, 2004, **82**, 93–108.

24 **Jackson, K. E.** Impact testing and simulation of a crashworthy composite fuselage concept. *Int. J. Crashworthiness*, 2001, **6**(1), 107–121.

25 **Tho, C. H., Sparks, C. E.,** and **Sareen, A. K.** Hard surface and water impact simulations of two helicopter subfloor concepts. American Helicopter Society 60th Annual Forum, Baltimore, MD, 7–10 June 2004.

26 **CAST.** Crashworthiness of helicopters onto water – Design of structures using advanced simulation tools. Funded by the European Community under the Competitive and Sustainable Growth Programme (Contract G4RD-CT1999-0172), 2000–2003.

27 **Pentecôte, N.** and **Vigliotti, A.** Simulation of the impact on water of a subfloor component and a full scale WG30 helicopter. American Helicopter Society 58th Annual Forum, Montréal, Canada, 11–13 June 2002.

28 **Hughes, K.** *Application of improved Lagrangian techniques to helicopter impacts on water*. PhD Thesis, Cranfield University, 2005.

29 **Pentecôte, N.** and **Vigliotti, A.** Crashworthiness of helicopters on water: test and simulation of a full-scale WG30 impacting on water. *Int. J. Crashworthiness*, 2003, **8**(6), 559–572.

30 **Kohlgrüber, D., Vigliotti, A., Weissberg, V.,** and **Bartosch, H.** Numerical simulation of a composite helicopter subfloor structure subjected to a water impact. American Helicopter Society 60th Annual Forum, Baltimore, MD, 8–10 June 2004.

31 **Oster, R.** D3.2.4 Post test report of 2nd helicopter sub floor drop test on rigid surface. Internal CAST report: Task 3.2/ECD/3.2.4, July 2001.